

***M*-shell x-ray production cross sections in thick targets of Ir, Pt, and Pb by 0.4–2.2-MeV $^4\text{He}^+$ ions**

R. Gowda and D. Powers

Department of Physics, Baylor University, Waco, Texas 76798

(Received 16 May 1984)

M-shell x-ray production cross sections in thick targets of Ir, Pt, and Pb have been measured for $^4\text{He}^+$ ions of energy from 0.4 to 2.2 MeV in steps of 0.1 MeV. The cross sections are compared with plane-wave Born approximation (PWBA) calculations and with perturbed-stationary-state calculations with energy-loss, Coulomb deflection, and relativistic corrections (ECPSSR). The present measurements, in general, agree well with the PWBA predictions at all energies, but agree with the ECPSSR theory only at projectile energies ≥ 1.5 MeV. The *M*-subshell x-ray cross sections are also calculated by a nonlinear (iterative) least-squares-fitting algorithm by extracting the relative line intensities of the experimentally observed spectra obtained with a Si(Li) detector. The subshell cross sections are compared with the scaled cross sections based on PWBA calculations. Good agreement is obtained for the case of M_1 , M_2 , and M_4 , and a larger deviation is found for M_3 and M_5 . The double nodal structure of the $3s$ -electron wave functions is confirmed, and the single inflection associated with the $3p_{3/2}$ -electron wave functions is not clearly visible in our data. The *M*-subshell cross-section ratios for $M_1/(M_2+M_3)$, $M_1/(M_4+M_5)$, and $(M_2+M_3)/(M_4+M_5)$ are also calculated, compared with the PWBA and ECPSSR theories, and discussed.

INTRODUCTION

The measurement of inner-shell ionization by charged particles has gained impetus because of the direct use of the particle-induced x-ray analysis method in many applied fields such as trace-element analysis,^{1,2} ion implantation,^{3–5} and fusion diagnostic studies.^{6,7} Direct Coulomb ionization is the dominant process responsible for inner-shell vacancies created in heavy atoms by light-ion impact. Among the various inner shells, the *K*- and *L*-shell ionization has been studied and understood both experimentally and theoretically to a great extent.^{8–10} The wave functions of the $2s$ and $2p$ electrons in these *L* shells have different shapes. The two different spin states of $2p$ electrons have similar wave functions but differ in energy.^{11,12} A comparison of *L*-subshell ionization cross-section ratios, particularly L_1 to L_2 and L_1 to L_3 , has shown a dip to occur at low incident projectile energy. This dip corresponds to the $2s$ density node, which is a sensitive test to predict the correct wave function to use in the theoretical treatment. A correlation was observed between the $2s$ density node and the dominant impact parameter obtained from the approximate positions of the experimentally observed plateau in the L_1 ionization cross-section curves. However, *M*-shell measurements are scarce and most of these studies^{13–23} are confined to total *M*-shell cross section measurements which show considerable disagreement.

Although the *M*-shell ionization cross-section measurements were started in the 1960's with the use of flow-type proportional counters^{13–15} as photon detectors, more precise measurements using high-resolution detectors began to appear only in the 1970's and afterwards.^{16–25} The important factors in measuring the *M*-shell ionization cross sections are detector efficiencies and various corrections

applied to the attenuation of x rays along their path prior to absorption in the detector-sensitive area. Relative radiative decay rates, fluorescence yields, and Coster-Kronig factors are important parameters involved in comparing the measured x-ray production cross sections. The complex nature of the *M*-shell x-ray ionization due to the small energy differences in the emitted x-ray lines, thus causing an overlapping of the lines, makes the study of *M*-subshell ionization cross sections more difficult. Already established methods for the calculation of detector efficiencies are employed.²³ The relative decay rates, fluorescence yields, and Coster-Kronig factors are obtained from the theoretical calculations of Bhalla²⁶ and McGuire.²⁷ The resolution of Si(Li) detectors (150–190 eV) is not sufficient to resolve the *M*-subshell x-ray line intensities, although a nonlinear (iterative) least-squares-fitting algorithm computer program^{28–30} can be used for this purpose.

The first *M*-subshell studies were made by Sarkar *et al.*,²⁴ who measured $M_{\alpha+\beta}$, M_γ , $M_2N_4M_3O_{1,4,5}$ lines of target elements $Z_2 = 62–79$ for incident proton beam energy of 250–400 keV. The x-ray production cross section of these lines was compared with the semiclassical approximation³¹ (SCA) and plane-wave Born approximation^{32–34} (PWBA) theories. The general shape of the PWBA curve agreed well with their experimental results. However, the SCA curve increased more steeply than the PWBA curve and the experimental curve, and this difference increased at higher projectile energies.

The next *M*-shell measurement was by de Castro Faria *et al.*,²⁵ who obtained *M*-subshell and total x-ray production cross sections of Au, Pb, Bi, and U for proton energies between 0.3 and 4.0 MeV. They measured the cross sections for the *M* lines M_5N_7 , M_4N_6 , M_3O_5 , M_2N_4 , and $M_1O_{2,3} + M_1P_{2,3}$ for each of the four targets. In ad-

dition, the M_3N_5 for Pb was also measured. They scaled their values as a universal function for the $3s$, $3p$, and $3d$ subshells for different values of η/θ^2 , where θ and η are the scaled binding energy and incident energy, respectively, and then made comparison with PWBA predictions. Their total cross sections were found to agree fairly well with PWBA predictions; their universal functions also agreed well for the case of M_1 , M_2 , and M_4 , but deviated more for M_3 and M_5 . These deviations were attributed to the calculated values of fluorescence yields.

In the present study an attempt has been made to measure the M -subshell x-ray production cross sections in thick targets of Ir, Pt, and Pb with an incident $^4\text{He}^+$ -ion energy of 0.4 to 2.2 MeV. The use of a nonlinear least-squares-fitting algorithm computer program allows at least 10 lines corresponding to 15 transitions to be isolated, and also allows the corresponding relative line intensities to be obtained. These relative intensities are used to calculate the M -subshell x-ray cross sections. The measured relative intensities are much more accurate than absolute intensities, since they are not influenced by normalization uncertainties. Furthermore, the ratios of subshell ($3s$, $3p$, and $3d$) cross sections have been calculated and compared with PWBA predictions and discussed to reveal the specific effects of the $3s$ electron wave functions. In addition, the total M -shell x-ray production cross sections have been compared with available experimental values and with the PWBA and recent ECPSSR (perturbed-stationary-state calculations with energy-loss, Coulomb deflection, and relativistic corrections) theories.³⁵

EXPERIMENTAL

The Baylor University 2.0-MeV Van de Graaff accelerator was used to produce the $^4\text{He}^+$ -ion beam. The ion beam was energy and mass analyzed by a calibrated magnet. Two suppressor rings were installed on the ends of the beam collimator to suppress the secondary electrons from it, so that this system could be used for thick target measurements. A positive bias of 300 V was applied to an insulated target rod to eliminate secondary-electron emission from the target. The $^4\text{He}^+$ ions collected on the target rod were converted to a current pulse using an ORTEC 439 digital current integrator in conjunction with an ORTEC 771 timer-counter. The timer-counter output pulse was used to gate an EG&G model 7150 multichannel analyzer (MCA) to record the x-ray spectrum for an arbitrary preset current rate. The recorded spectrum was stored in a VAX computer for further analysis and data reduction. The M x-rays were detected with an ORTEC Si(Li) detector positioned at 135° to the incident-beam direction and 90° to the target plane. During the experiment, the vacuum was always maintained at about 6×10^{-6} Torr. The detector was positioned outside the target chamber and subtended a solid angle of 0.54 msr from the target foil.

The Si(Li) detector had an energy resolution of 174 eV at 5.9 keV, an active diameter of 6 mm, and a sensitive depth of 5 mm. The dead layer on the silicon crystal was $0.1 \mu\text{m}$ with a 200-Å-thick gold layer on it and was covered with a 0.0127-mm-thick beryllium window. A 1-

cm-thick air column existed between the 0.20-mm-thick Mylar window of the scattering chamber and the detector. Pileup effects in the detector electronics were avoided by keeping the count rate low (dead time less than 10%) by use of a 5–20-nA He^+ beam current on the target rod. Elemental thick targets of Ir and Pt of 99.9% purity, and thick targets of Pb, were obtained from J. Bishop & Co., Malvern, PA, and A. D. Mackay, Darien, CT, respectively. The M x-ray spectra recorded with Si(Li) detector did not reveal any impurity characteristic x-ray lines.

DATA ANALYSIS

The analysis of the spectra was made by a nonlinear (iterative) least-squares-fitting algorithm. The data analysis program assumes Gaussian peaks and fits the function $F(x)$ to every collection of overlapping peaks as follows:

$$F(x) = B(x) + \sum_{i=1}^N G_i(x), \quad (1)$$

where $B(x)$ is the background function, $G_i(x)$ is the i th Gaussian peak of the collection, x is the channel number of the MCA, and N is the number of overlapping peaks. $G_i(x)$ has the form

$$G_i(x) = a_1 \exp\{-4 \ln 2 [(x - a_2)/a_3]^2\}, \quad (2)$$

where a_1 is the height, a_2 is the centroid, and a_3 is the full width at half maximum of the peak. The background function assumes a linear background with a finite slope. Since the peak width is a function of energy, care has been taken to incorporate this variation with the x-ray energies. In a few cases where the differences were small compared to the peak width, a single peak was assumed. The uncertainties of background, peak height, and positions are given by the covariance matrix which is calculated by the least-squares-fitting algorithm.

A typical M x-ray spectrum of Ir for 1.2 MeV $^4\text{He}^+$ ions is shown in Fig. 1. As can be seen in the figure, we

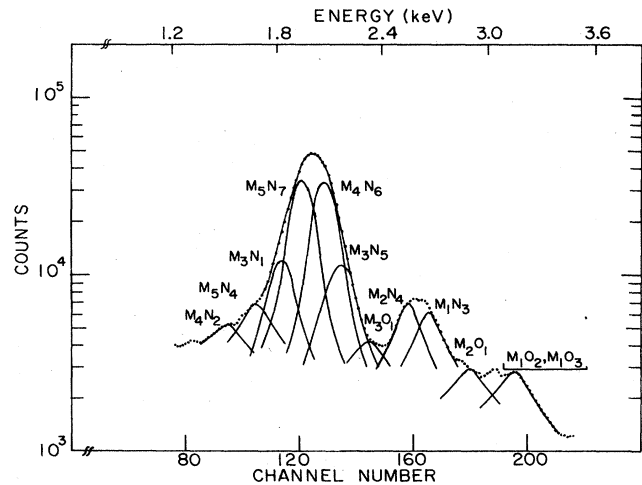


FIG. 1. M x-ray spectrum of Ir produced by 1.2-MeV $^4\text{He}^+$ ions. The decomposition of the spectrum for selected transitions is also shown. The transitions M_4N_2 , M_5N_7 , M_3N_5 , and M_2N_4 include M_5N_3 , M_5N_6 , $M_3N_4 + M_2N_1$, and M_1N_2 , respectively.

have identified M_4N_2 , M_5N_4 , M_3N_1 , M_5N_7 , M_4N_6 , M_3N_5 , M_3O_1 , M_2N_4 , M_1N_3 , M_2O_1 , and $M_1O_2 + M_1O_3$ transitions. In the case of Pt and Pb, M_3O_1 was not observed. In the figure some of the peaks contain contributions from other transitions which have negligibly small energy differences. Thus, the peaks are identified only by the dominant transitions. M_4N_2 , M_5N_7 , and M_2N_4 contain contributions from M_5N_3 , M_5N_6 , and M_1N_2 , respectively, and M_3N_4 contains M_2N_1 and M_3N_5 . The theoretical branching ratios²⁶ were used to find the individual contribution to that subgroup. Finally, the profile for each peak was corrected for detection efficiency and then used to build up the x-ray yields for each subgroup M_i ($i=1-5$).

The calculation of the M -subshell x-ray production cross sections was made by use of the formula given by Basbas *et al.*³⁶ (under the assumption that all M_i x-ray lines are emitted isotropically):

$$\sigma_M^x(E_1) = \frac{4\pi}{n\Omega\epsilon} \left[\left. \frac{dY(E'_1)}{dE'_1} \right|_{E'_1=E_1} S(E_1) + \mu \frac{\cos\Theta}{\cos\Phi} Y(E_1) \right], \quad (3)$$

where n is the number density of the target atoms, Ω is the solid angle, ϵ is the efficiency of the Si(Li) detector; $Y(E_1)$ is the M_i x-ray yield per incident particle, $dY(E'_1)/dE'_1$ is the slope evaluated at $E'_1=E_1$, $S(E_1)$ is the stopping power, μ is the absorption coefficient of the target for its own M x-ray lines, and Θ and Φ are the angles between the normal to the target surface

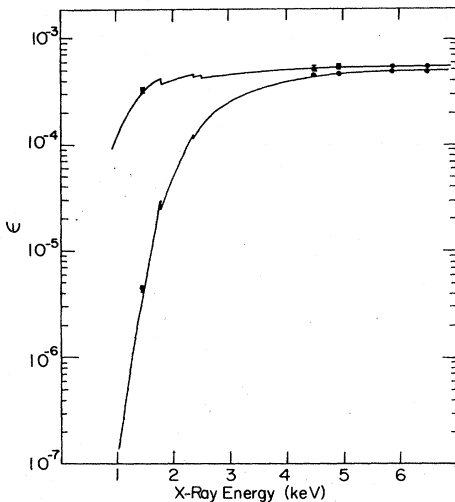


FIG. 2. Si(Li) detector efficiency ϵ as a function of x-ray energy in keV. Both curves are obtained from Eq. (4) in the text, where use has been made of Viegele's mass attenuation coefficients (Ref. 44). The upper curve includes attenuation from the Au layer, Si dead layer, and Be window on the detector. The lower curve includes these same attenuation contributions along with additional attenuation from the 0.02-mm-thick Mylar window and 1-cm-thick air column between the scattering chamber and the Si(Li) detector. The five experimental points on each curve are obtained as outlined in the text.

and, respectively, the incident beam direction and the line between target beam spot and detector. We have taken $\Theta = \Phi = 45^\circ$. With regard to the isotropic emission of x rays, Schöller and Bell³⁷ indicate that all K radiation should be emitted isotropically but that Cu L and Ge L radiation show polarization fractions of less than 4% for 100-keV proton impact. Lewis *et al.*³⁸ found no anisotropy for Sn L radiation for 6.25-MeV/amu α particles and deuterons. Bernstein and Lewis³⁹ found Au L radiation to be isotropic within 2% for 1.5–4.25-MeV protons. No anisotropy measurements for M radiation exist, and we have, therefore, assumed isotropy in the calculation using the formula of Basbas *et al.*³⁶

The Si(Li) detector efficiency was determined by use of the $K\alpha$ lines of Al, Ti, and V induced by 1.0-MeV $^4\text{He}^+$ ion bombardment. Since recent K -shell ionization cross-section measurements for transition metal elements at 0.3–2.4-MeV proton bombardment agree well⁴⁰ with the ECPSSR theory,³⁵ we have used this theory to calculate K -shell ionization cross sections of Al, Ti, and V. These cross sections are used in the expression by Basbas *et al.*³⁶ along with stopping powers by Ziegler⁴¹ and the solid angle $\Omega = 0.54$ msr to obtain detector efficiency for x rays of energy 1.5, 4.5, and 4.95 keV, respectively. A calibrated ^{55}Fe source was also used to determine detector efficiency at 5.9 and 6.49 keV by procedures used in the literature.^{42,43} These five values of efficiency are plotted as the solid points with error estimates $\pm 8.6\%$ in Fig. 2. The upper and lower theoretical curves in Fig. 2 are calculated from

$$\epsilon = \epsilon_0 \exp \left[- \sum_i \mu_i x_i \right], \quad (4)$$

where ϵ and ϵ_0 are detector efficiencies with and without attenuation, respectively; μ_i is the mass attenuation coefficient obtained from Viegele,⁴⁴ and x_i is the i th attenuation coefficient for the Au layer (200 Å), Si dead layer (0.1 μm), and Be window (0.0127 mm) for the Si(Li) detector. Both curves are normalized to the ^{55}Fe 5.9 $K\alpha$ line; the lower curve is identical to the upper curve except that it also includes attenuation from the 0.02-mm-thick Mylar window and the 1-cm-thick air column between the scattering chamber and Si(Li) detector.

The experimental uncertainties vary from 9% to 11% and come mainly from detector efficiency, transmission corrections, and solid-angle corrections ($\sim 8\%$). The counting statistics were very small in most cases ($< 1\%$). The background subtraction introduces up to 2% error. The slope of the yield curve, dY/dE , is known better than to $\pm 5\%$ error. In determining the relative peak intensities, errors no greater than 4% were observed. The stopping-power cross sections and x-ray absorption coefficients will introduce additional uncertainties of (5–10)% in addition to the (9–11)% overall error given above.

RESULTS AND DISCUSSION

The measured total M -shell x-ray production cross sections for $^4\text{He}^+$ ions on Ir, Pt, and Pb targets are presented as a function of projectile energy in Table I. The theoretical M -shell ionization cross sections (σ_M^I) must be converted into x-ray production cross sections (σ_M^x) using the fluorescent yields ω_i , Coster-Kronig transition factors

TABLE I. Experimental M -shell x-ray production cross sections (barns).

He ⁺ -ion energy (MeV)	Ir	Target Pt	Pb
0.4			20
0.5	67		40
0.6	102		68
0.7	157	150	107
0.8	218	212	148
0.9	281	269	200
1.0	365	344	251
1.1	446	419	301
1.2	522	505	350
1.3	663	580	419
1.4	711	615	460
1.5	764	724	501
1.6	850	786	537
1.7	933	888	620
1.8	985	944	669
1.9	1021	1016	760
2.0	1113	1056	807
2.1	1175	1110	865
2.2	1239	1140	901

(f_{ij}), and the super-Coster-Kronig factors (S_{ij}) (Ref. 27) in order to make a comparison between the experimental and the PWBA and ECPSSR theories. The following relations are used for this purpose:

$$\sigma_{M_1}^I = (1/\omega_1)\sigma_{M_1}^X, \quad (5)$$

$$\sigma_{M_2}^I = (1/\omega_2)\sigma_{M_2}^X - S_{12}\sigma_{M_1}^I, \quad (6)$$

$$\sigma_{M_3}^I = (1/\omega_3)\sigma_{M_3}^X - S_{23}\sigma_{M_2}^I - (S_{13} + S_{12}S_{23})\sigma_{M_1}^I, \quad (7)$$

$$\begin{aligned} \sigma_{M_4}^I = & (1/\omega_4)\sigma_{M_4}^X - S_{34}\sigma_{M_3}^I - (S_{24} + S_{23}S_{34})\sigma_{M_2}^I \\ & - (S_{14} + S_{12}S_{24} + S_{13}S_{34} + S_{12}S_{23}S_{34})\sigma_{M_1}^I, \end{aligned} \quad (8)$$

$$\begin{aligned} \sigma_{M_5}^I = & (1/\omega_5)\sigma_{M_5}^X - f_{45}\sigma_{M_4}^I - (S_{35} + S_{34}f_{45})\sigma_{M_3}^I \\ & - (S_{25} + S_{23}S_{35} + S_{24}f_{45} + S_{23}S_{34}f_{45})\sigma_{M_2}^I \\ & - (S_{15} + S_{12}S_{25} + S_{13}S_{35} + S_{14}f_{45} + S_{12}S_{23}S_{35} \\ & + S_{12}S_{24}f_{45} + S_{13}S_{34}f_{45} + S_{12}S_{23}S_{34}f_{45})\sigma_{M_1}^I. \end{aligned} \quad (9)$$

The total M -shell cross sections can be obtained as

$$\sigma_M^X = \sum_{i=1}^5 \sigma_{M_i}^X. \quad (10)$$

In Fig. 3 the total M -shell x-ray production cross sections are compared with the PWBA and ECPSSR calculations. The PWBA calculations are based on the universal function $F_{3l}(\eta/\theta^2, \theta)$ tabulated by Johnson *et al.*³⁴ The ECPSSR theoretical values are calculated by Lapicki.⁴⁵ For the case of Pb, the present thick-target measurements are also compared with the thin target measurements of

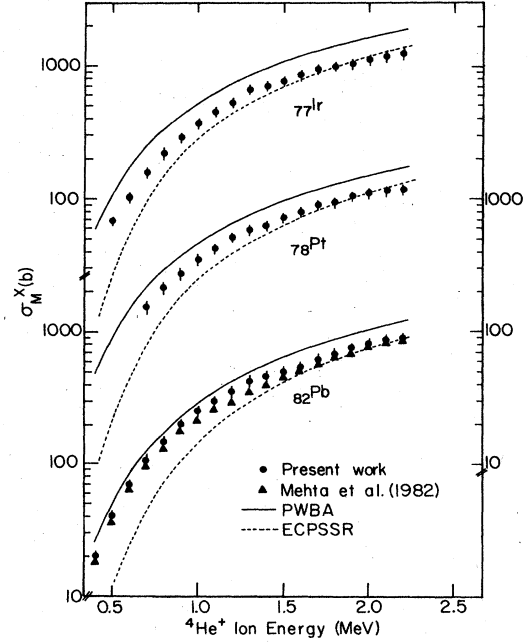


FIG. 3. M -shell x-ray production cross sections for Ir, Pt, and Pb as a function of ${}^4\text{He}^+$ -ion energy. The errors are the (9–11)% ones stated in the text. The PWBA and ECPSSR theoretical curves for the three target elements are also shown. In the case of Pb the thin-target measurements of Mehta *et al.* (Ref. 23) are given.

Mehta *et al.*²³ It can be seen from the figure that the experimental values for Pb from the two different laboratories give fairly good agreement (< 10% difference) for low projectile energy (up to 0.6 MeV) and for high projectile energies (≥ 1.5 MeV), but differ by as much as 20% for 1.1–1.4-MeV ${}^4\text{He}^+$ ions. This disagreement in Pb is not uncharacteristic of measurements by different experimental groups. In fact, the same proton thin-target measurements by Mehta *et al.*²³ for Au, Pb, Bi, and U for 0.3–2.6-MeV protons are lower by 30% in Au and 13% for Pb, Bi, and U than those of de Castro Faria *et al.*²⁵ The present experimental values for Pb and Pt agree with the PWBA predictions within 30% over the entire energy region, but for Ir below 1 MeV the difference between PWBA and experiment becomes as large as 40%. On the other hand, the present measurements for Ir, Pt, and Pb agree well (within 20%) above 1.5 MeV with the ECPSSR calculations. Below 1.5 MeV, however, the present values for Pb and those of Mehta *et al.*²³ for Pb show a large deviation which increases from about 25% at 1.4 MeV to a factor of 4.6 to 0.4 MeV. The Pt and Ir measurements follow a similar, but not nearly as drastic, trend and differ by 10% at 1.4 MeV to about 80% at 0.6 MeV. From the figure to some extent, one can observe a sort of Z_2 dependence between the measurements and ECPSSR predictions in which the difference increases with increasing Z_2 . The difference between the present experimental values and the PWBA calculations, however, shows a reverse trend in which the difference decreases with increasing Z_2 . The deviations between experiment and ECPSSR at

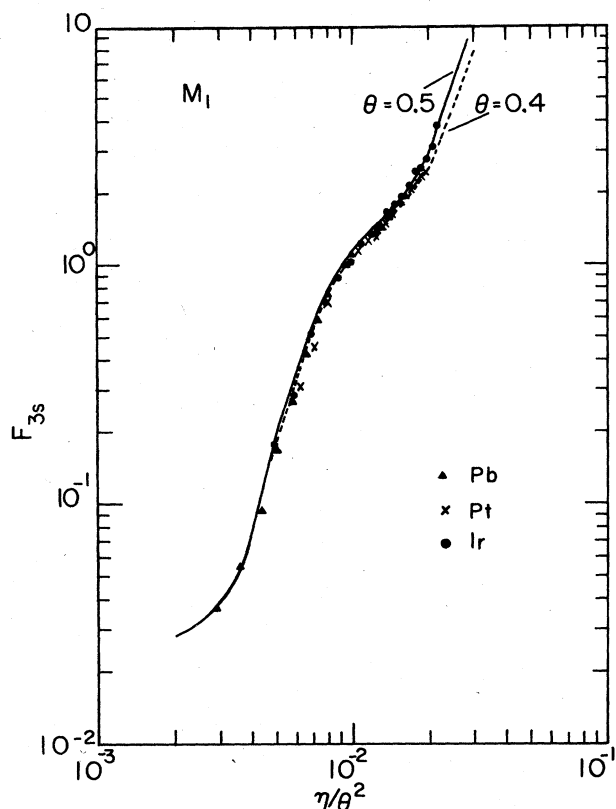


FIG. 4. Scaled experimental M_1 ionization cross sections for Ir, Pt, and Pb are compared with PWBA theoretical curves for two different values of θ . The parameters η and θ are defined in the text.

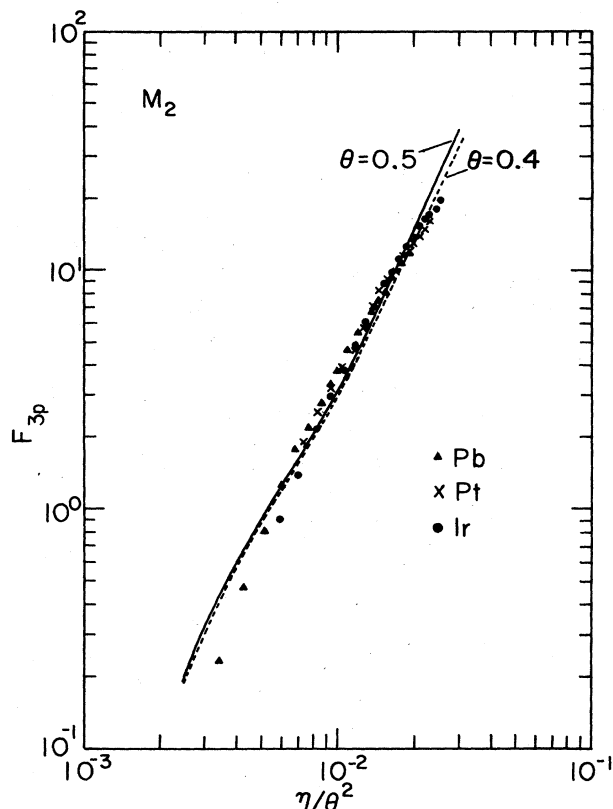


FIG. 5. Same as Fig. 4 for M_2 .

lower energies cannot be attributed conclusively to any one factor. The target thickness is not that decisive because in Pb the thin-target measurements of Mehta *et al.*²³ agree reasonably well with our thick-target measurements.

For the case of M -subshell cross sections, our experimental cross sections have been converted to the scaled ionization cross sections or to the universal function³⁴ $F_{31}(\eta/\theta^2, \theta)$ using the statistical weights of the $3s$, $3p$, and $3d$ electrons. The parameter θ is the scaled binding energy $\hbar\omega n^2/Z^2\mathcal{R}$, where $n=3$ for the M subshell; $\hbar\omega$ is the observed binding energy for the M electrons; $Z=Z_2-11.25$ for the M_1 , M_2 , and M_3 subshells; $Z=Z_2-21.15$ for the M_4 and M_5 subshells, and $\mathcal{R}=13.6$ eV. The quantity $\eta=v_1^2/(Zv_0)^2$ is the scaled projectile energy parameter, where v_1 is the He^+ -ion velocity, $v_0=e^2/\hbar$, and Z is defined as in the parameter θ . These values are compared with those made from PWBA predictions³⁴ and are presented in Figs. 4–8. It is seen from the figures that except for M_3 and M_5 , once again a fairly good agreement is found. Particularly for Ir, M_5 shows a large deviation.

In Fig. 4, the M_1 subshell exhibits very clearly the double inflection which reflects the two nontrivial nodes of the $3s$ electron wave functions, which was referred to by de Castro Faria *et al.*²⁵ In Fig. 6, a slight evidence exists

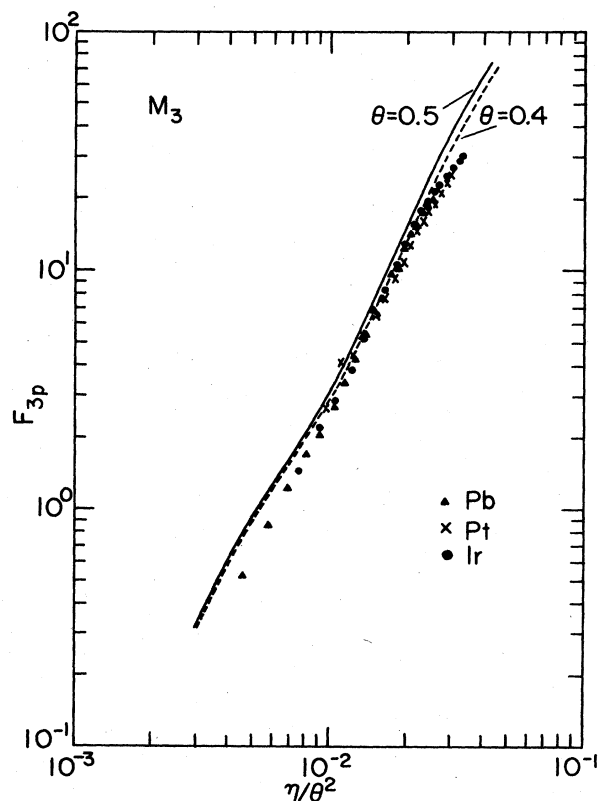
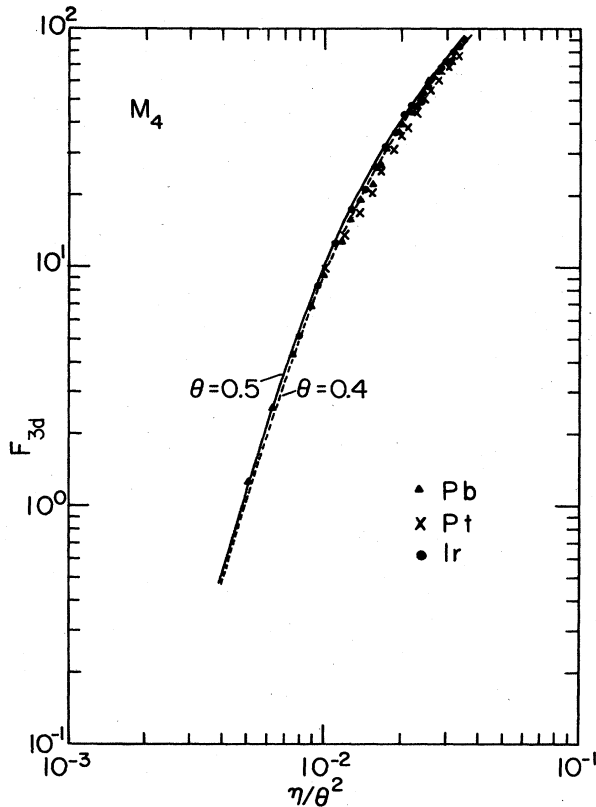
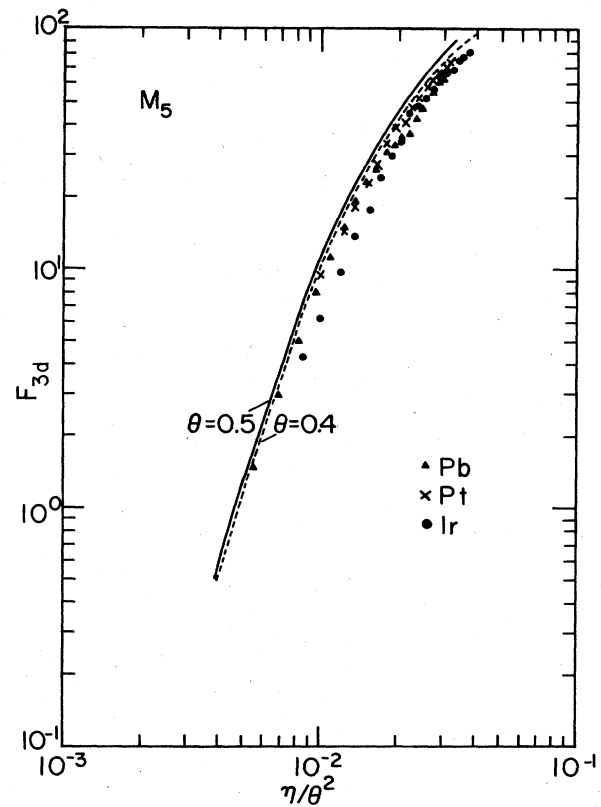


FIG. 6. Same as Fig. 4 for M_3 .

FIG. 7. Same as Fig. 4 for M_4 .FIG. 8. Same as Fig. 4 for M_5 .

in the experimental measurements for the single inflection association with the $3p_{3/2}$ electron wave functions although perhaps not as strong as anticipated by the theory.

Most of the systematic errors involved in the measurements of the x-ray yields can be eliminated by working with cross-section ratios. In Fig. 9 we plot the cross-section ratios against the projectile energy for both measured and theoretically calculated PWBA and ECPSSR values for the cases of $M_1/(M_2+M_3)$ ($3s/3p$), $M_1/(M_4+M_5)$ ($3s/3d$), and $(M_2+M_3)/(M_4+M_5)$ ($3p/3d$). The ratios show a well-pronounced energy dependence. For the ($3s/3p$) ratio in all three targets, fair agreement between theory and experiment can be observed in the peak area region between the higher energy dip and lower energy dip, which are labeled in reverse order as inner and outer node, respectively. The $^4\text{He}^+$ -ion energies used in the present experiment (0.4–2.2 MeV) are insufficient to cover both dips for all three targets unambiguously; nevertheless, the inner node at 1.6 MeV in Ir and the outer node at 0.5 MeV and Pb are clearly visible in the ($3s/3p$) ratios plotted in the left portion of Fig. 9. In the region between the two nodes the experimental ($3s/3p$) ratios agree rather well with the PWBA calculated values, and not quite as well with the ECPSSR predictions. Also, in the ($3s/3p$) ratio, it is seen that as Z_2 increases, the peak position between the two nodes shifts towards higher incident energies. The PWBA peak position is slightly lower in energy (0.1 MeV) than the ECPSSR value. These ($3s/3p$) peak position energies, which change with the no-

dal positions for different elements, give the same ratio of 0.862 between the scaled velocity and the scaled binding energy η/θ .

The ratio $M_1/(M_4+M_5)$ ($3s/3d$) in the middle portion of Fig. 9 reveals clearly the dips corresponding to the outer nodal position for Pb at 0.6 MeV and the inner nodal position for Ir at 1.6 MeV for the $3s$ electron wave function. Fairly good agreement between both PWBA and ECPSSR theories and experiment is seen for the outer node at 0.6 MeV for Pb, and qualitative agreement between both theories and experiment for the inner node at 1.6 MeV for Ir is also observed. A systematic difference of $\approx 30\%$ between experiment and both theories for the ($3s/3d$) ratio in Ir is seen in the middle portion of Fig. 9. There is also approximately a 10% difference in the peak region for Pt, but a larger difference ($\approx 30\%$) exists for the inner nodal position at 1.6 MeV. A similar trend in increasing peak position energy with Z_2 and peak position values at $\eta/\theta=0.655$ is observed for these ($3s/3d$) ratios. In the right portion of the figure (Fig. 9) the $(M_2+M_3)/(M_4+M_5)$ ($3p/3d$) ratios are also plotted. A fair agreement between the experiment and the two theories is observed for all three target elements.

In conclusion, the deviations between the PWBA theory and experiment for total M x-ray production cross sections are believed to be mainly due to the various normalization parameters (detector efficiency, photon attenuation coefficients, and stopping-power cross sections) and calculated atomic parameters (relative radiative decay rates,

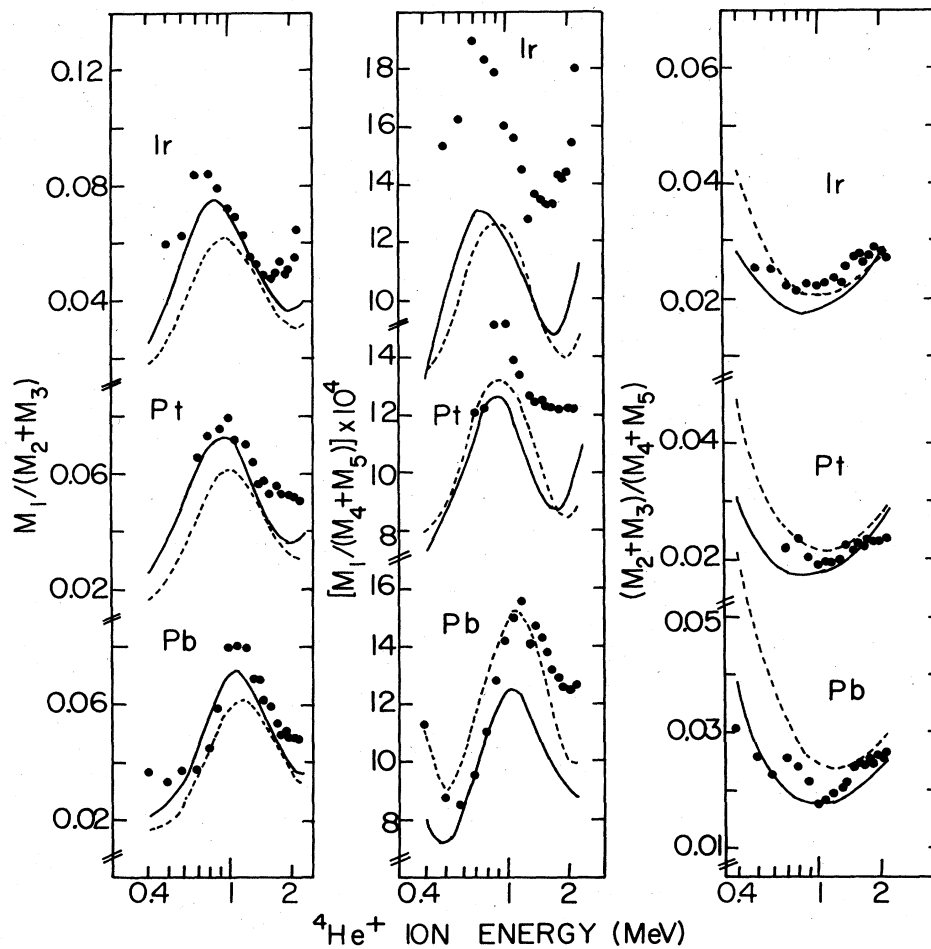


FIG. 9. Plot of M -subshell x-ray production cross-section ratios $M_1/(M_2+M_3)$, $M_1/(M_4+M_5)$, and $(M_2+M_3)/(M_4+M_5)$ vs the projectile energy. The solid curves are the PWBA calculations, and the dotted curves are the ECPSSR calculations of Lapicki (Ref. 45).

fluorescence yields, and Coster-Kronig transition rates) because of the uniform (30–40)% disagreement between theory and experiment over the entire energy region. The target thickness may be part of the difference but because ionization cross-section measurements by different groups using thin targets differ by magnitudes greater than the thin-target–thick-target difference in Pb, we feel that this is unlikely. The ECPSSR theory gives good agreement for ${}^4\text{He}^+$ projectiles only in the energy region above 1.5 MeV. This is the region where the projectile velocity is equal to or greater than the orbital velocities of the M -shell electrons. The Mehta *et al.*²³ measurements are consistently lower than the ECPSSR predictions for higher projectile velocities. The reason for the large difference between experiment and ECPSSR below 1 MeV is unknown, unless the energy-loss correction and Coulomb corrections may perhaps be excessive. It is our conclusion that the ECPSSR predictions are fair in the region where the projectile velocity is close to the M -shell electron velocities in the target atom.

The present x-ray production cross-section ratio studies reveal that the effects of electrons in different subshells are clearly visible. The peak between the two dips is a

consequence of the double nodal structure in the $3s$ wave functions. Both the PWBA and ECPSSR calculations predict rather well both energy position and height of the maxima, and their width agrees well with the present experimental values with few exceptions. For the M_1 subshell ($3s$) the double inflection which reflects the two non-trivial nodes of the $3s$ electron wave functions is clearly revealed in our data as seen in Fig. 4, but for M_3 , the single inflection associated with the $3p_{3/2}$ electrons is not pronounced clearly in Fig. 6. In particular, the fluorescence yield used to calculate the M_5 subshell x-ray production cross section is responsible for making the PWBA predictions too large in Fig. 8.

ACKNOWLEDGMENTS

The work was supported by the Robert A. Welch Foundation of Houston, Texas, under Grant No. AA-264. The authors are grateful for the support of the Welch Foundation through the years. They are also particularly grateful to Professor Gregory Lapicki for graciously providing his ECPSSR calculations for Ir, Pt, and Pb. We are also grateful to Mr. Kar Chun Charles Lok for his kind assistance in the computational work.

- ¹T. B. Johansson, R. Akselsson, and S. A. E. Johansson, *Nucl. Instrum. Methods* **84**, 141 (1970).
- ²K. R. Akselsson, *IEEE Trans. Nucl. Sci.* **NS-28**, 1370 (1981).
- ³L. J. Christensen, J. M. Khan, and W. F. Brunner, *Rev. Sci. Instrum.* **38**, 20 (1967).
- ⁴T. J. Gray, R. Lear, R. J. Dexter, F. N. Schwettmann, and K. C. Weimer, *Thin Solid Films* **19**, 103 (1973).
- ⁵B. D. Sartwell, A. B. Campbell III, B. S. Covino, Jr., and T. J. Driscoll, *IEEE Trans. Nucl. Sci.* **NS-26**, 1670 (1979).
- ⁶B. M. Johnson, K. W. Jones, J. L. Cecchi, and T. H. Kruse, *IEEE Trans. Nucl. Sci.* **NS-26**, 1317 (1979).
- ⁷J. Kilwer and A. Elfiqi, *IEEE Trans. Nucl. Sci.* **NS-26**, 1323 (1979).
- ⁸*Methods of Experimental Physics*, edited by P. Richard (Academic, New York, 1980), Vol. 17, p. 228.
- ⁹R. K. Gardner and T. J. Gray, *At. Data Nucl. Data Tables* **21**, 515 (1978).
- ¹⁰H. Paul, *At. Data Nucl. Data Tables* **24**, 243 (1979); *IEEE Trans. Nucl. Sci.* **NS-28**, 1119 (1981).
- ¹¹E. L. B. Justiniano, A. A. G. Nader, N. V. de Castro Faria, C. V. Barros Leite, and A. G. de Pinho, *Phys. Rev. A* **21**, 73 (1980).
- ¹²E. Rosato, *Phys. Rev. A* **28**, 2759 (1983).
- ¹³R. C. Jopson, H. Mark, and C. D. Swift, *Phys. Rev.* **127**, 1612 (1962).
- ¹⁴J. M. Khan, D. L. Potter, and R. D. Worley, *Phys. Rev.* **135**, A511 (1964); **136**, A108 (1964); **139**, A1735 (1965); **163**, 81 (1967).
- ¹⁵P. B. Needham, Jr. and B. D. Sartwell, *Phys. Rev. A* **2**, 27 (1970); **2**, 1686 (1971).
- ¹⁶C. E. Busch, A. B. Baskin, P. H. Nettles, S. M. Shafroth, and A. W. Waltner, *Phys. Rev. A* **7**, 1601 (1973).
- ¹⁷K. Ishii, S. Morita, H. Tawara, H. Kaji, and T. Shiokawa, *Phys. Rev. A* **11**, 119 (1975).
- ¹⁸V. S. Nikolaev, V. P. Petukhov, E. A. Romanovsky, V. A. Sergeev, I. M. Kruglova, and V. V. Beloshitsky, *The Physics of Electronic and Atomic Collisions* (University of Washington, Seattle, 1975), p. 419.
- ¹⁹S. T. Thornton, R. H. McKnight, and R. R. Karlowicz, *Phys. Rev. A* **10**, 219 (1974).
- ²⁰M. Poncet and Ch Engelman, *Nucl. Instrum. Methods* **159**, 455 (1979).
- ²¹K. Sera, K. Ishii, A. Yamadera, A. Kuwako, M. Kamya, M. Sebata, S. Morita, and T. C. Chu, *Phys. Rev. A* **22**, 2536 (1980).
- ²²R. Mehta, J. L. Duggan, J. L. Price, P. M. Kocur, and F. D. McDaniel, *Phys. Rev. A* **28**, 3217 (1983).
- ²³R. Mehta, J. L. Duggan, J. L. Price, F. D. McDaniel, and G. Lapicki, *Phys. Rev. A* **26**, 1883 (1982).
- ²⁴M. Sarkar, H. Mommsen, W. Sarter, and P. Schürkes, *J. Phys. B* **14**, 3163 (1981).
- ²⁵N. V. de Castro Faria, F. L. Freire, Jr., A. G. de Pinho, and E. F. da Silveira, *Phys. Rev. A* **28**, 2770 (1983).
- ²⁶C. P. Bhalla, *J. Phys. B* **3**, 916 (1970).
- ²⁷E. J. McGuire, *Phys. Rev. A* **5**, 1043 (1972).
- ²⁸D. W. Marquardt, *J. Soc. Ind. Appl. Math.* **11**, 431 (1963).
- ²⁹F. B. Smith and D. F. Shanno, *Technometrics* **13**, 63 (1971).
- ³⁰E. Marageter, W. Wegscheider, and K. Müller, *Nucl. Instrum. Methods Phys. Res. B* **1**, 137 (1984).
- ³¹J. M. Hansteen, O. M. Johnsen, and L. Kocbach, *At. Data Nucl. Data Tables* **15**, 306 (1975).
- ³²G. S. Khandewal, B. H. Choi, and E. Merzbacher, *At. Data* **1**, 103 (1969).
- ³³B. H. Choi, *Phys. Rev. A* **7**, 2056 (1973).
- ³⁴D. E. Johnson, G. Basbas, and F. D. McDaniel, *At. Data Nucl. Data Tables* **24**, 1 (1979).
- ³⁵W. Brandt and G. Lapicki, *Phys. Rev. A* **23**, 1717 (1981).
- ³⁶G. Basbas, W. Brandt, and R. Laubert, *Phys. Rev. A* **7**, 983 (1973).
- ³⁷A. Schöller and F. Bell, *Z. Phys. A* **286**, 163 (1978).
- ³⁸C. W. Lewis, R. L. Watson, and J. B. Natowitz, *Phys. Rev. A* **5**, 1773 (1972).
- ³⁹E. M. Bernstein and H. W. Lewis, *Phys. Rev.* **95**, 83 (1954).
- ⁴⁰M. D. Brown, D. G. Simons, D. J. Land, and J. G. Brennan, *Phys. Rev. A* **25**, 2935 (1982).
- ⁴¹J. F. Ziegler, *Helium, Stopping Powers and Ranges in all Elemental Matter*, (Pergamon, New York, 1977), Vol. 4.
- ⁴²J. S. Hansen, J. G. McGeorge, D. Nix, W. D. Schmidt-Ott, I. Unus, and R. W. Fink, *Nucl. Instrum. Methods* **106**, 365 (1973).
- ⁴³J. L. Campbell and L. A. McNelles, *Nucl. Instrum. Methods* **117**, 519 (1974); **125**, 205 (1975).
- ⁴⁴W. J. Viegele, *At. Data* **5**, 1 (1973).
- ⁴⁵G. Lapicki (private communication).